
Article:
Cao, T., Lu, B., Ou, H. et al. (2 more authors) (2016) Investigation on a new hole-flanging approach by incremental sheet forming through a featured tool. International Journal of Machine Tools and Manufacture, 110. pp. 1-17. ISSN 0890-6955

https://doi.org/10.1016/j.ijmachtools.2016.08.003

International Journal of Machine Tools & Manufacture, Vol. 110(2016), pp. 1–17

http://dx.doi.org/10.1016/j.ijmachtools.2016.08.003

Investigation on a new hole-flanging approach by incremental sheet forming through a featured tool

Tingting Cao[a], Bin Lu[a, b], Hengan Ou[c], Hui Long[b], Jun Chen[a*]

a Department of Plasticity Technology, Shanghai JiaoTong University, Shanghai, 200030, China
b Department of Mechanical Engineering, University of Sheffield, Sheffield S1 3JD, UK
c Department of Mechanical, Materials and Manufacturing Engineering, University of Nottingham, Nottingham, NG7 2RD, UK

*Corresponding author. E-mail address: jun_chen@sjtu.edu.cn (J. Chen).

Abstract

One of the major challenges in conventional incremental sheet forming (ISF) is the extreme sheet thinning resulted in an uneven thickness distribution of formed part. This is also the case for incrementally formed parts with hole-flanging features. To overcome this problem, a new ISF based hole-flanging processing method is proposed by developing a new ISF flanging tool. Comparative studies are conducted by performing hole-flanging tests using both ISF conventional ball-nose tool and the new flanging tool to evaluate the sheet deformation behavior and the quality of the final part. Stress distribution and strain variation are investigated by analytical approach and numerical simulation. Experiments have been conducted to validate the analytical model and simulation results, and to further study the fracture behavior. Results show that the new flanging tool generates greater meridional bending than stretching deformation in conventional ISF. The combination of bending-dominated deformation mode with localized deformation of ISF ensures more uniform thickness distribution on hole-flanging part with better resistance to fracture.

Keyword: incremental sheet forming; hole-flanging; tool path; flanging tool.

International Journal of Machine Tools & Manufacture, 110 (2016), pp. 1–17
http://dx.doi.org/10.1016/j.ijmachtools.2016.08.003

Nomenclature

σ_{ϕ}^{C}	Meridional stress under the ball-nose tool
σ_{θ}^{C}	Circumferential stress under the ball-nose tool
σ_{t}^{C}	Thickness stress under the ball-nose tool
σ_{m}^{C}	Hydrostatic stress under the ball-nose tool
η^{C}	Stress triaxiality under the ball-nose tool
R^{C}	Tool radius of the ball-nose tool
σ_{ϕ}^{B}	Meridional stress under the new flanging tool
σ_{θ}^{B}	Circumferential stress under the new flanging tool
σ_{t}^{B}	Thickness stress under the new flanging tool
σ_{m}^{B}	Hydrostatic stress under the new flanging tool
η^{B}	Stress triaxiality under the new flanging tool
R^{B}	Tool radius of the new flanging tool
σ_{Y}	Yield stress
α	Forming angle in the meridional direction
θ	Contact angle in the circumferential direction
r	Distance between element A and the central axis during deformation
l	Distance between element A and the central axis before deformation
r_0	Distance between the edge of the contact area and the central axis
t_0	Initial sheet metal thickness
t	Actual sheet thickness of element A
μ_{ϕ}	Frictional coefficient along the meridional direction
μ_{θ}	Frictional coefficient along the circumferential direction

1. Introduction

Hole-flanging is a typical sheet forming process to produce flange features on sheet metal parts. In the conventional hole-flanging process, a sheet metal blank or component with a small pre-cut hole is punched to form a cylindrical or conical flange. This process involves sheet bending and stretching deformation locally around the pre-cut hole. Conventional hole-flanging process has been extensively studied and well developed. The earlier investigation on this process can be traced back to late 1960s. Baldin et al. [1] investigated the flanging coefficient, forming load and change of material microstructure in the hole-flanging process. Since 1970s, various flanging processes have been developed. Johnson et al. [2] reported a quasi-static drifting and punching process for hole-flanging, the sheet metal deformation behavior and the corresponding forming load were investigated using punches with different head shapes. Kumagai and Saiki [3] investigated a combined hole-flanging and ironing process for thick sheet metals. Kumagai et al. [4] also developed a hole-flanging and ironing process for sheet metal made of Al/Cu bi-metallic sheet metal layers. Worswick and Finn [5] developed a new flanging method by a stretching process and compared the “simple stretch flange” with the “z stretch flange” process. It was found that the necking instabilities occurred at lower strain values in the z-flange process as compared with the simple stretch flange process. Groche and Erhardt [6] introduced laser heating into hole-flanging process to improve the formability of magnesium and aluminum alloys.

The above studies mainly focused on traditional hole-flanging process, in which the punch is statically fixed on the ram of a press. Other technologies with rotating punch have also been developed, by utilizing the thermal effect, Head et al. [7] patented a flow drilling process to create holes with bushing in sheet metal. This technology was particularly suitable for the fabrication of thin sheets or tubes without backing support. Miller and Shih [8] further studied this flow drilling process by measuring forming load, tool wear and final microstructure in the sheet metal part. Allwood and Shouler [9] developed a paddle forming process to produce sheet metal parts with pronounced features and increased formability by taking the advantages from the effect of through thickness shear. Allwood and Shouler [10] further studied the effect of through thickness shear and suggested that it was the major cause for the increased formality in paddle forming. These two technologies have further enhanced the process capability of hole-flanging.

In recent years, incremental sheet forming (ISF) process has become a promising technique in flexible forming of sheet metal parts. During ISF process, a stylus-type tool moves along a predefined tool path to form a sheet metal part with 3D complex freeform surfaces. This process does not require any dedicated forming tool with a specific geometrical shape or a forming press. In addition, the ISF technology also exhibits a higher formability compared with conventional sheet forming processes. Malhotra et al. [11] suggested that

the increased formability by ISF was caused by localized and incremental deformation of the sheet, which could avoid the occurrence of necking. Considering these advantages, ISF process has become a viable alternative to conventional punching process in manufacturing of small-batch or customized sheet metal parts, especially in the fields of aerospace, biomedical and automotive applications. Concerning the hole-flanging by ISF, various technologies have been developed in recent years. Teramae et al. [12] proposed a new incremental burring process for manufacturing the branched tube, and the effect of the material properties on the wall thickness distribution was studied. Cui and Gao [13] developed an ISF hole-flanging process by employing three multi-pass ISF toolpath strategies, and they compared the thickness distributions of the parts obtained by the three different forming strategies. Petek and Kuzman [14] proposed a backward ISF hole-flanging process. In this process, the tool head size was larger than that of the tool shank diameter, which was different from conventional ISF tools. Yang et al. [15] proposed a similar bar tool with larger tool head to produce thin-walled flange features on the tubes. Recently, Bambach et al. [16] developed a hole-flanging tool with adaptive blank holder to improve the geometrical accuracy. The above works have further extended the process flexibility of hole-flanging by ISF.

Concerning the investigation on ISF based hole-flanging processes, Centeno et al. [17] found that the material deformation mode in ISF hole-flanging was different from conventional ISF without a pre-cut hole, in which the sheet deformation was a combination of in-plane stretching and bending at the perimeter of the flange. Centeno et al. [18] also investigated the failure mode in ISF hole-flanging process and found that the improved formability was due to the suppression of necking before fracture. Montanari et al. [19] investigated the sheet deformation in ISF hole-flanging process and found that the sheet around hole edge experienced equal bi-axial stretching. Cristino et al. [20] traced the strain evolution in ISF hole-flanging process and predicted the fracture by ductile damage modeling. Cristino et al. [21] also investigated ISF hole-flanging with square features which had improved the understanding of material plastic deformation and processing failure in fabrication of square parts. Concerning forming non-metallic materials such as polymer, Silva et al. [22] studied the feasibility of forming polyethylene terephthalate sheet by ISF hole-flanging process. Yonan et al. [23] investigated the ISF and ISF hole-flanging processes on PVC and found that strain measurement is an effective way to determine the accumulated damage of PVC parts. These studies have further improved the understanding of material deformation and fracture in the ISF based hole-flanging process.

Although the ISF hole-flanging process shows great potentials, one major limitation is the extreme sheet thinning of the formed part. In previous research, Centeno et al. [18] confirmed that meridional stretching was the major deformation mode before the tool reached the hole edge, which unavoidably caused the

thinning of formed rim. Recently, Cristino et al. [24] compared the hole-flanging by punching and ISF processes. They observed different strain paths in the sheet metal deformations of the two processes, and revealed different deformation mechanisms between conventional punching and ISF. In conventional hole-flanging by the press and die, the flange rim is generally thicker but shorter in depth. For ISF hole-flanging part, the flange rim has greater depth but with thinner thickness. This phenomenon was also observed by Silva et al. [25]. Uneven thickness distribution becomes a main obstacle for ISF hole-flanging to directly replacing traditional hole-flanging processes in industrial applications. Therefore, how to produce flange features with increased process flexibility and required shape and thickness accuracy is a new challenge in promoting ISF applications.

To minimise the sheet thinning in ISF hole-flanging process, a new featured flanging tool is developed in this study. With the new tool geometry, the thinning caused by sheet stretching can be minimised. To evaluate the deformation behavior and the final flanging part quality formed by the new tool, comparative studies have been conducted by performing ISF hole-flanging using conventional ball-nose tool and the new flanging tool. The comparison studies look into key aspects of the final part geometry, the thickness distribution, the forming load and the hole-expansion ratio. To obtain a better understanding of the ISF hole-flanging process, material deformation mechanisms under the above two tools are studied by analytical, numerical and experimental approaches. The detailed stress states and strain histories, the cause of improved thickness distribution and fracture under these two tools are investigated and discussed. The advantages and new challenge of the new ISF flanging tool are also discussed to reach key conclusions.

2. Development of the featured flanging tool

For all reported ISF-based hole-flanging processes, a ball-nose tool is usually employed to make the material deform around the edge of pre-cut hole via different toolpath strategies [13]. If the conventional ISF toolpath strategy is employed, the tool will move from the periphery of the sheet metal inward to the hole edge. Following this strategy, the sheet metal deforms similarly as that in ISF deformation mode of stretching with bending around the tool, which unavoidably leads to severe sheet metal thinning.

To achieve a uniform sheet thickness deformation in ISF based hole-flanging processes, a new featured tool is proposed as shown in Fig. 1. This new flanging tool consists of some geometric features including the hyperbolic and cylindrical sections below the tool arm. Even though the pre-cut hole is usually prepared by blanking with shearing or by laser cutting. But for hole-flanging process by ISF based on CNC milling machine, milling cutter is the more suitable tool which can simplify the required tool and equipment. In this situation,

the milling cutter can be incorporated at the tip of the tool so that the initial hole can be made without replacing the tools during the ISF flanging process. Three major geometric parameters R^B, $H_1{}^B$and $H_2{}^B$ are used to define the profile of the tool head.

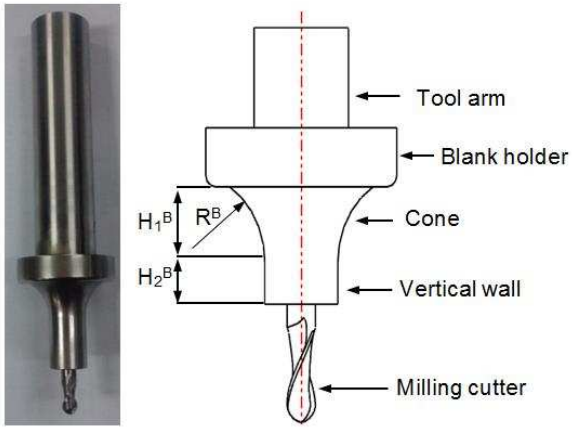

Fig. 1. The design of the new featured flanging tool.

Fig. 2 shows the tool path strategy used for ISF-based hole-flanging processes by using conventional ball-nose tool (T1) and new flanging tool (T2). T1 travels from the periphery of the sheet towards the pre-cut hole moving down along a 3D profile layer by layer in the Z-direction. In the process using tool T1, point to point contact typically occurs between the tool and sheet metal. However for the process using T2, the tool moves from inward to outward along a tool path horizontally in the X-Y plane. In this process, the contact between tool and sheet metal is typically along a vertical “band” area region, as shown in Fig. 2(b). With moving the tool outward, the sheet metal will deform gradually and the hole will be “expanded” to form a flange feature. In Fig. 2, the red points show the starting points for the two different tool path strategies.

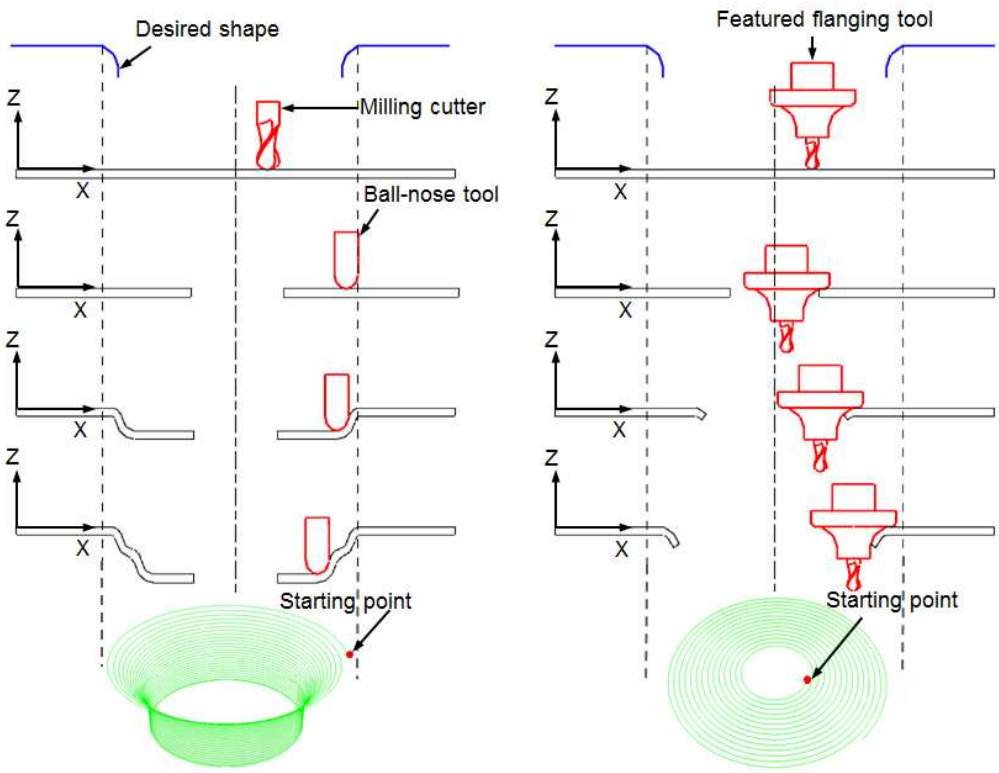

(a) T1 (b) T2

Fig. 2. Different hole-flanging tool path strategies.

3. Analytical study of the two ISF hole-flanging processes

During ISF hole-flanging process, T1 and T2 have different tool moving strategies, which results in a varied tool-sheet contact and boundary conditions. These will further affect the stress and deformation state or even formability of the sheet. To understand difference of deformation mechanism caused by T1 and T2, analytical studies are conducted first to compare sheet stress distributions of the two hole-flanging processes. Conventional ISF governing equations [26] are employed for the process using T1, while new equations are established for the process using T2 to investigate the stress distributions.

3.1 The ball-nose tool - T1

During the ISF hole-flanging process using the ball-nose tool (T1), the tool moves along a 3D spiral tool path to form the sheet metal part incrementally layer by layer. A selected element *A* is chosen for stress analysis, as shown in Fig. 3(a). Three stress components σ_t^C, σ_θ^C and σ_ϕ^C are defined in the principle directions of *t*, θ and ϕ, as shown in Fig. 3(c) and (d), respectively. Point *O* is defined as a point on the central axis of the forming sheet and point O_1 is on the center axis of the ball head of the tool. In addition, the following assumptions are made:

(1) Membrane approach is employed, as the sheet metal is rather thin compared to the tool radius, typically the ratio of sheet thickness to the tool ball head radius is 0.2.

(2) σ_t^C is independent of θ, the gradient of thickness stress in the circumferential direction is ignored since the major effect of circumferential friction is the circumferential stress.

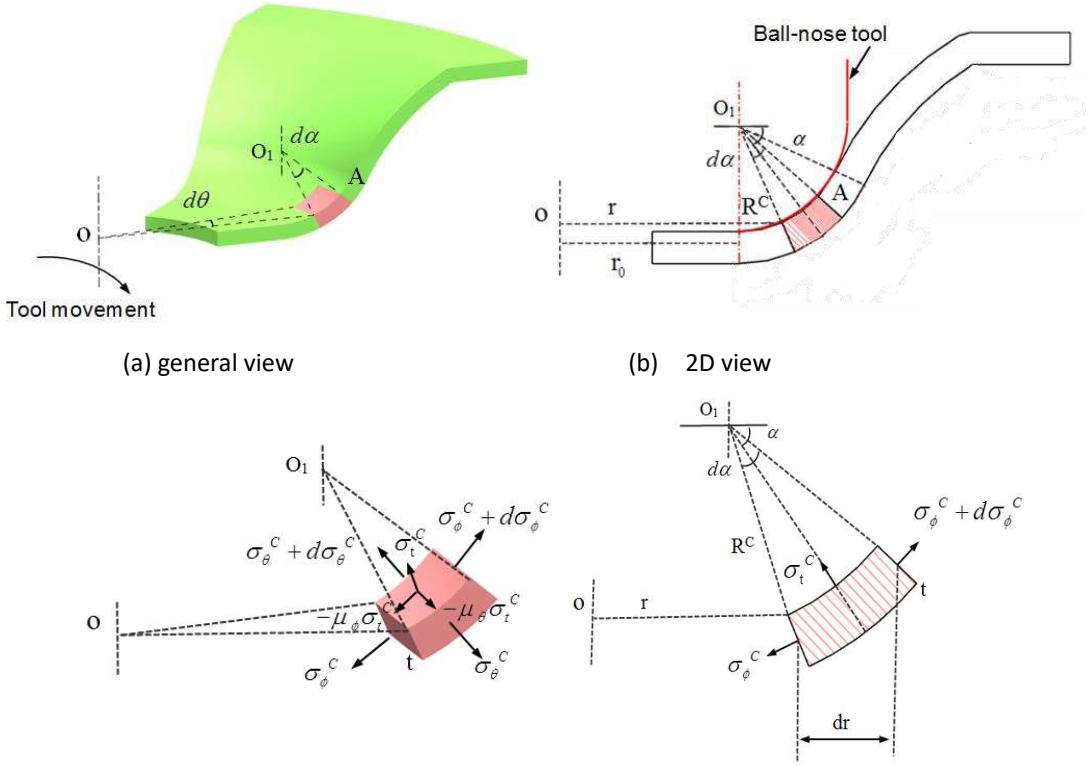

(a) general view (b) 2D view

(c) Stress components of 3D element A (d) Stress components of 2D element *A*

Fig. 3. Schematic representation of hole-flanging process by ball-nose tool (T1).

According to our previous research [26], the stress components in three principle directions can be given by:

$$\sigma_t^C = \frac{t}{-2\mu_\theta \cdot r \cdot \theta - 2t} \cdot \sigma_Y \quad (1)$$

$$\sigma_\phi^C = \frac{-2\mu_\theta \cdot r \cdot \theta - t}{-2\mu_\theta \cdot r \cdot \theta - 2t} \cdot \sigma_Y \quad (2)$$

$$\sigma_\theta^C = \frac{-\mu_\theta \cdot r \cdot \theta}{-2\mu_\theta \cdot r \cdot \theta - 2t} \cdot \sigma_Y \quad (3)$$

From the principle stresses, the hydrostatic stress in the selected element can be expressed as:

$$\sigma_m^C = \frac{\sigma_t^C + \sigma_\theta^C + \sigma_\phi^C}{3} = \frac{1}{3}\left(\frac{t}{-2r\mu_\theta\theta - 2t}\sigma_y + \frac{-r\mu_\theta\theta}{-2r\mu_\theta\theta - 2t}\sigma_y + \frac{-2r\mu_\theta\theta - t}{-2r\mu_\theta\theta - 2t}\sigma_y\right) \quad (4)$$

Accordingly, the stress triaxiality in the ISF flanging process using T1 can be written as:

$$\eta^{C} = \frac{\sigma_m{}^{C}}{\sigma_Y} = \frac{-\mu_\theta \cdot r \cdot \theta}{-2\mu_\theta \cdot r \cdot \theta - 2t} \tag{5}$$

According to the geometrical relationship shown in Fig. 3(b), the distance from element A to the central axis of the forming sheet can be given by:

$$r = r_0 + R^{C} \cos\alpha \tag{6}$$

Considering the Sine law $t = t_0 \sin\alpha$, Eqs. (2), (3) and (5) can be further expressed as:

$$\sigma_\phi{}^{C} = \frac{-2\mu_\theta \cdot \theta \cdot (r_0 + R^{C}\cos\alpha) - t_0 \sin\alpha}{-2\mu_\theta \cdot \theta \cdot (r_0 + R^{C}\cos\alpha) - 2t_0 \sin\alpha} \cdot \sigma_Y \tag{7}$$

$$\sigma_\theta{}^{C} = \frac{-\mu_\theta \cdot \theta \cdot (r_0 + R^{C}\cos\alpha)}{-2\mu_\theta \cdot \theta \cdot (r_0 + R^{C}\cos\alpha) - 2t_0 \sin\alpha} \cdot \sigma_Y \tag{8}$$

$$\eta^{C} = \frac{\sigma_m{}^{C}}{\sigma_Y} = \frac{-\mu_\theta \cdot \theta \cdot (r_0 + R^{C}\cos\alpha)}{-2\mu_\theta \cdot \theta \cdot (r_0 + R^{C}\cos\alpha) - 2t_0 \sin\alpha} \tag{9}$$

The above stress components will be calculated and used to make comparison with that derived by using T2.

3.2 The new ISF flanging tool -T2

Membrane analysis approach will also be employed to investigate the ISF process using the new flanging tool (T2) as shown in Fig. 4. The stress components $\sigma_t{}^{B}$, $\sigma_\theta{}^{B}$ and $\sigma_\phi{}^{B}$ are also defined in the directions of *t*, θ, ϕ as shown in Fig. 4(c) and (d), respectively. Point *O* is also a point on the central axis of the forming and point O_1 is at the center of the arc in the section of forming tool.

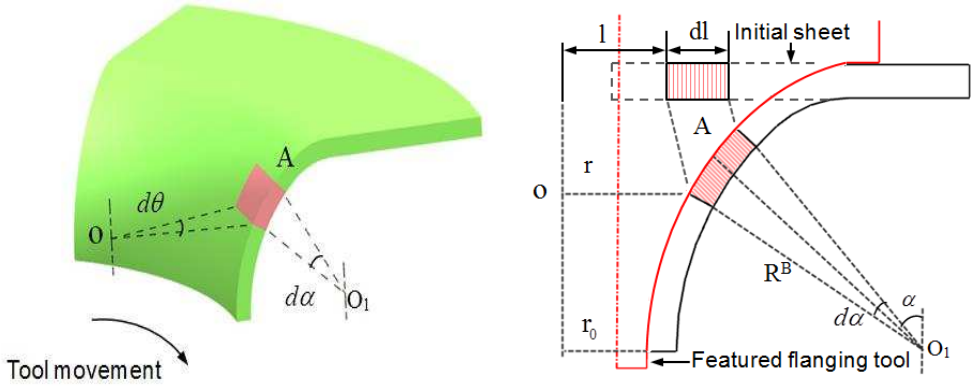

(a) general view (b) 2D sectional view

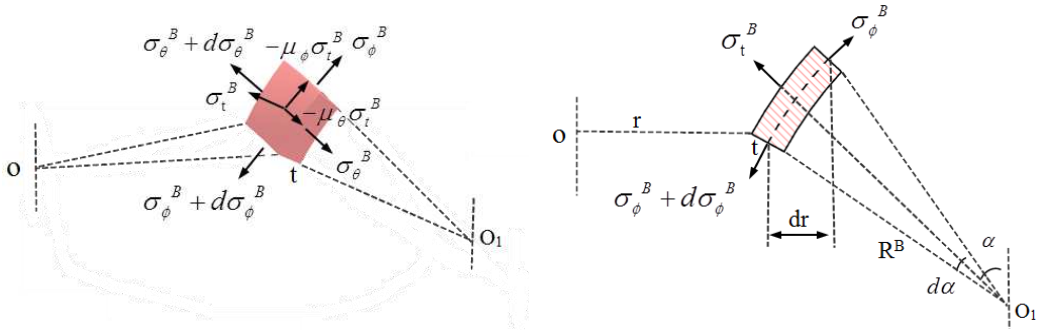

(c) Stress components in 3D element *A* (d) Stress components in 2D element A

Fig. 4. Schematic representation of hole-flanging process by using T2.

Concerning the stress state along the meridional direction, the equilibrium equation can be given by:

$$\sigma_\phi^{\mathrm{B}}\mathrm{t}(\mathrm{r}+\mathrm{dr})\mathrm{d}\theta\cos(\mathrm{d}\alpha/2)-\mathrm{t}(\sigma_\phi^{\mathrm{B}}+\mathrm{d}\sigma_\phi^{\mathrm{B}})\mathrm{r}\mathrm{d}\theta\cos(\mathrm{d}\alpha/2)$$
$$-\mu_\phi\sigma_{\mathrm{t}}^{\mathrm{B}}\mathrm{r}\mathrm{R}^{\mathrm{B}}\mathrm{d}\alpha\mathrm{d}\theta-2\mathrm{t}(\sigma_\theta^{\mathrm{B}}+\mathrm{d}\sigma_\theta^{\mathrm{B}})\mathrm{R}\mathrm{d}\alpha\sin(\mathrm{d}\theta/2)\cos\alpha=0 \quad (10)$$

By neglecting higher order infinitesimal terms, Eq. (10) can be simplified as:

$$\mathrm{d}\sigma_\phi^{\mathrm{B}}=\frac{\sigma_\phi^{\mathrm{B}}-\sigma_\theta^{\mathrm{B}}}{\mathrm{r}}\mathrm{dr} \quad (11)$$

Along the thickness direction, the equilibrium condition can be given by:

$$\sigma_{\mathrm{t}}^{\mathrm{B}}\mathrm{R}^{\mathrm{B}}\mathrm{r}\mathrm{d}\theta\mathrm{d}\alpha+\sigma_\theta^{\mathrm{B}}\mathrm{R}^{\mathrm{B}}\mathrm{t}\sin(\mathrm{d}\theta/2)\sin\alpha\mathrm{d}\alpha+\mathrm{t}(\sigma_\theta^{\mathrm{B}}+\mathrm{d}\sigma_\theta^{\mathrm{B}})\mathrm{R}^{\mathrm{B}}\sin(\mathrm{d}\theta/2)\sin\alpha\mathrm{d}\alpha$$
$$-\sigma_\phi^{\mathrm{B}}\mathrm{t}\cdot\mathrm{r}\sin(\mathrm{d}\alpha/2)\mathrm{d}\theta-(\sigma_\phi^{\mathrm{B}}+\mathrm{d}\sigma_\phi^{\mathrm{B}})(\mathrm{r}+\mathrm{dr})(\mathrm{t}+\frac{\mathrm{dt}}{2})\sin(\mathrm{d}\alpha/2)\mathrm{d}\theta=0 \quad (12)$$

Considering that $\sin(\mathrm{d}\alpha/2)\approx\mathrm{d}\alpha$ and $\sin(\mathrm{d}\theta/2)\approx\mathrm{d}\theta$, Eq. (12) can be simplified as:

$$\sigma_{\mathrm{t}}^{\mathrm{B}}\mathrm{r}\mathrm{R}^{\mathrm{B}}+\sigma_\theta^{\mathrm{B}}\mathrm{R}^{\mathrm{B}}\mathrm{t}\sin\alpha-\sigma_\phi^{\mathrm{B}}\mathrm{r}\mathrm{t}+\frac{1}{2}\mathrm{d}\sigma_\theta^{\mathrm{B}}\mathrm{R}^{\mathrm{B}}\mathrm{t}\sin\alpha-\frac{1}{2}\sigma_\phi^{\mathrm{B}}\mathrm{d}\mathrm{r}\mathrm{t}$$
$$-\frac{1}{2}\mathrm{d}\sigma_\phi^{\mathrm{B}}\mathrm{r}\mathrm{t}-\frac{1}{2}\mathrm{d}\sigma_\phi^{\mathrm{B}}\mathrm{t}\mathrm{d}\mathrm{r}-\frac{1}{4}\sigma_\phi^{\mathrm{B}}\mathrm{r}\mathrm{d}\mathrm{t}-\frac{1}{4}\sigma_\phi^{\mathrm{B}}\mathrm{d}\mathrm{r}\mathrm{d}\mathrm{t}-\frac{1}{4}\mathrm{d}\sigma_\phi^{\mathrm{B}}\mathrm{r}\mathrm{d}\mathrm{t}-\frac{1}{4}\mathrm{d}\sigma_\phi^{\mathrm{B}}\mathrm{d}\mathrm{r}\mathrm{d}\mathrm{t}=0 \quad (13)$$

By neglecting high order infinitesimal terms, Eq. (13) can be simplified as:

$$\frac{\sigma_{\mathrm{t}}^{\mathrm{B}}}{\mathrm{t}}+\frac{\sigma_\theta^{\mathrm{B}}\sin\alpha}{\mathrm{r}}-\frac{\sigma_\phi^{\mathrm{B}}}{\mathrm{R}^{\mathrm{B}}}=0 \quad (14)$$

Using Tresca criterion $\sigma_\theta^{\mathrm{B}}-\sigma_{\mathrm{t}}^{\mathrm{B}}=\sigma_{\mathrm{Y}}$ with an assumption of $\frac{\sin\alpha}{\mathrm{r}}<<\frac{1}{\mathrm{t}}$, Eq. (14) can be derived as:

$$\frac{\sigma_{\mathrm{t}}^{\mathrm{B}}}{\mathrm{t}}+\frac{\sigma_{\mathrm{Y}}.\sin\alpha}{\mathrm{r}}=\frac{\sigma_\phi^{\mathrm{B}}}{\mathrm{R}^{\mathrm{B}}} \quad (15)$$

Substituting Tresca criterion and Eq. (15) to Eq. (11), Eq. (16) can be obtained as:

$$d\sigma_{\phi}^{B}=(\frac{R^{B}}{rt}\sigma_{t}^{B}+\frac{R^{B}+r_{0}-r}{r^{2}}\sigma_{Y}-\frac{\sigma_{t}^{B}}{r}-\frac{\sigma_{Y}}{r})dr \tag{16}$$

Integrating Eq.(16) at both sides and considering the boundary conditions that the meridional stress is nearly zero ($\sigma_{\phi}^{B}\approx 0$) at the hole edge ($r=r_{0}$), the meridional stress σ_{ϕ}^{B} can be expressed as:

$$\sigma_{\phi}^{B}=(\frac{R^{B}}{t}-1)\sigma_{t}^{B}\ln\frac{r}{r_{0}}-\frac{R^{B}+r_{0}}{r}\sigma_{Y}-2\sigma_{Y}\ln\frac{r}{r_{0}}+\frac{R^{B}+r_{0}}{r_{0}}\sigma_{Y} \tag{17}$$

Considering Tresca criterion, the circumferential stress σ_{θ}^{B} can also be expressed by σ_{t}^{B}:

$$\sigma_{\theta}^{B}=\sigma_{Y}+\sigma_{t}^{B} \tag{18}$$

Combining Eqs. (15) with (17), σ_{t}^{B} can be expressed by the key process parameters as follows:

$$\sigma_{t}^{B}=\frac{2\ln\frac{r}{r_{0}}+2\frac{R^{B}+r_{0}}{r}-\frac{R^{B}}{r_{0}}}{(\frac{R^{B}}{t}-1)\ln\frac{r}{r_{0}}-\frac{R^{B}}{t}}\cdot\sigma_{Y} \tag{19}$$

Therefore, the hydrostatic stress can be expressed as:

$$\begin{aligned}\sigma_{m}^{B}&=\frac{1}{3}(\sigma_{t}^{B}+\sigma_{\theta}^{B}+\sigma_{\phi}^{B})\\&=\frac{1}{3}\left\{[\left(\frac{R^{B}}{t}-1\right)\ln\frac{r}{r_{0}}+2]\sigma_{t}^{B}-\left(\frac{R^{B}+r_{0}}{r}+2\ln\frac{r}{r_{0}}-\frac{R^{B}+r_{0}}{r_{0}}-1\right)\sigma_{Y}\right\}\end{aligned} \tag{20}$$

And the stress triaxiality is represented as:

$$\eta^{B}=\frac{1}{3}\{[(\frac{R^{B}}{t}-1)\ln\frac{r}{r_{0}}+2]\cdot\frac{2\ln\frac{r}{r_{0}}+2\frac{R^{B}+r_{0}}{r}-\frac{R^{B}}{r_{0}}}{(\frac{R^{B}}{t}-1)\ln\frac{r}{r_{0}}-\frac{R^{B}}{t}}-(\frac{R^{B}+r_{0}}{r}+2\ln\frac{r}{r_{0}}-\frac{R^{B}+r_{0}}{r_{0}}-1)\} \tag{21}$$

To replace sheet metal thickness *t* and distance *r* in the above equation, the geometric relationship given in Eq. (22) is employed to determine the distance:

$$r=R^{B}(1-\sin\alpha)+r_{0} \tag{22}$$

In addition, Eq. (23) can be obtained based on the volume constancy:

$$2\pi l\cdot dl\cdot t_{o}=2\pi r\cdot R^{B}d\alpha\cdot t \tag{23}$$

Considering that $dl=R^{B}d\alpha$ and the deformation in the meridional direction is quite small, the assumption is made for:

$$l = R^B + r_o - \alpha \cdot R^B \tag{24}$$

The sheet metal thickness can be obtained as:

$$t = \frac{(R^B + r_o - \alpha \cdot R^B) \cdot t_o}{R^B(1-\sin\alpha) + r_0} \tag{25}$$

To analyze the stress distribution and stress triaxiality on the contact area between the tool and forming sheet, Eqs. (17), (18) and (21) can be further expressed by using the forming angle α based on Eqs. (22) and (25). The relationship between the stress state and the forming angle α will be analyzed in the later section.

3.3 Comparison of the stress distribution

Using Eqs. (7), (8), (17) and (18), the distributions of meridional stress and circumferential stress with varying forming angles and tool radii can be obtained. The process parameters used in the analysis are given in Table 1 to calculate the stress distribution of each process by using different hole-flanging tools.

Table 1 Parameters used in the analytical calculation.

Parameters	Value
r_0	25 mm
μ_θ	0.1
ϑ	30º
σ_Y	116 MPa
t_0	1 mm

The meridional stress and circumferential stress induced during hole-flanging processes using T1 and T2 are compared as shown in Fig. 5. It is found that the maximum principle stress with T1 is the meridional stress while that with T2 is the circumferential stress. With T1 used, both meridional stress and circumferential stress are in tensile state and they slightly increase with the decreasing of the forming angle, as shown in Fig. 5(a). However for T2, the two principle stress components are more sensitive to the changes of the process parameters, the meridional stress is in compressive state, and with the decrease of the forming angle, the meridional stress becomes even smaller. The circumferential stress is in tensile state and slightly decreases

with the decreasing of the forming angle. The comparison shows that T2 can result in varied stress state depending on the process parameters, while the stress state with T1 is more stable and insensitive to the changes of process parameters.

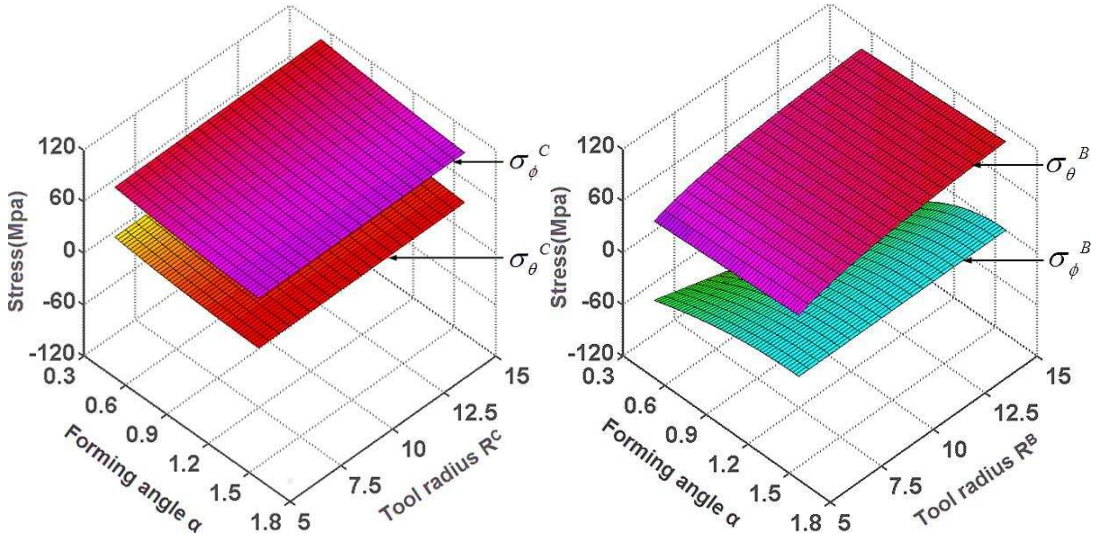

(a) T1 (b) T2

Fig. 5. The stress distribution for each hole-flanging process.

Stress triaxiality can be regarded as an indicator to evaluate the formability. Using Eqs. (9) and (21), the distribution of stress triaxiality under the varied forming angles and the tool radii during each process can be determined, as shown in Fig. 6. It can be seen in Fig. 6(a) that stress triaxiality η^C with T1 increases with the decreasing of the forming angle, which indicates that the fracture will first occur near the deformed inclined wall but not at the contact area between the tool and forming sheet. With T2, the stress triaxiality also decreases with the decreasing of forming angle. However, this trend is more obvious when the tool radius is relatively large. It suggests that the fracture may firstly occur at the hole edge, where the forming angle is the largest.

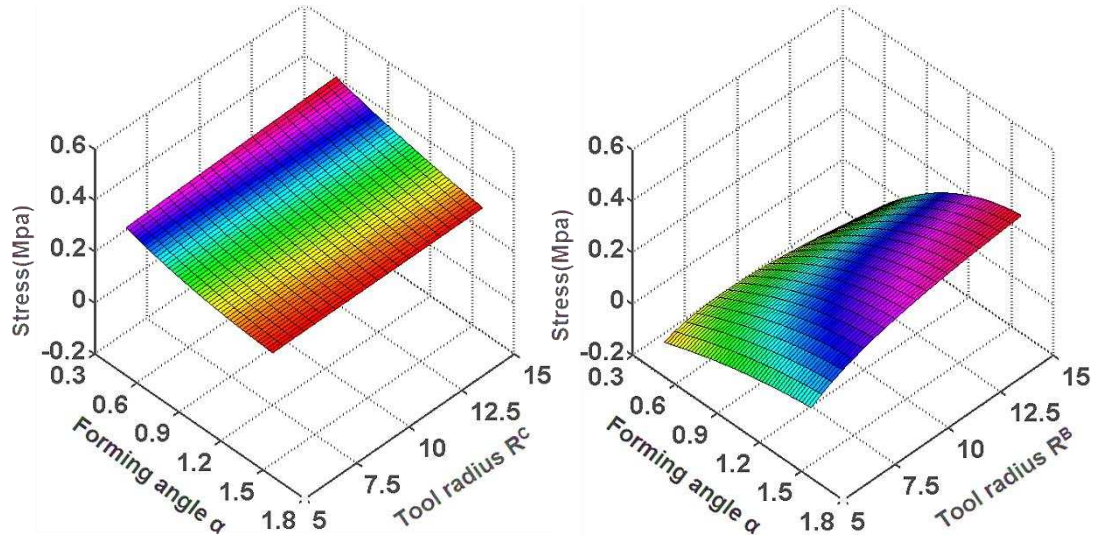

(a) T1 (b) T2

Fig. 6. The stress triaxiality for each hole-flanging process.

4. Numerical simulation

4.1 Finite element simulation

Numerical simulation is also conducted to investigate the strain distribution and to validate feasibility of the new flanging process. In this work, the hole-flanging processes using T1 and T2 are compared by forming a specific hole-flanging feature as shown in Fig. 7(a). In the conventional ISF hole-flanging process, T1 with a radius of 5 mm is employed. In the new hole-flanging process, the geometrical parameters of T2 shown in Fig. 1 are given in Table 2. AA5052 sheet metal with initial thickness of 1 mm is used in the simulation. The flow stress of the AA5052 sheet is given in Fig. 7(b). The most straightforward one-step spiral tool path with a constant step down value as 0.1 mm is adopted for the process with T1, while a spiral tool path with a constant gap of 0.1 mm between path loops in the X-Y plane is used for the process with T2.

Table 2 Geometrical dimensions of T2.

Parameters	Value
Tool radius R^B of T2	15 mm
Cone height H_1^B of T2	13 mm
Vertical wall height H_2^B of T2	15 mm

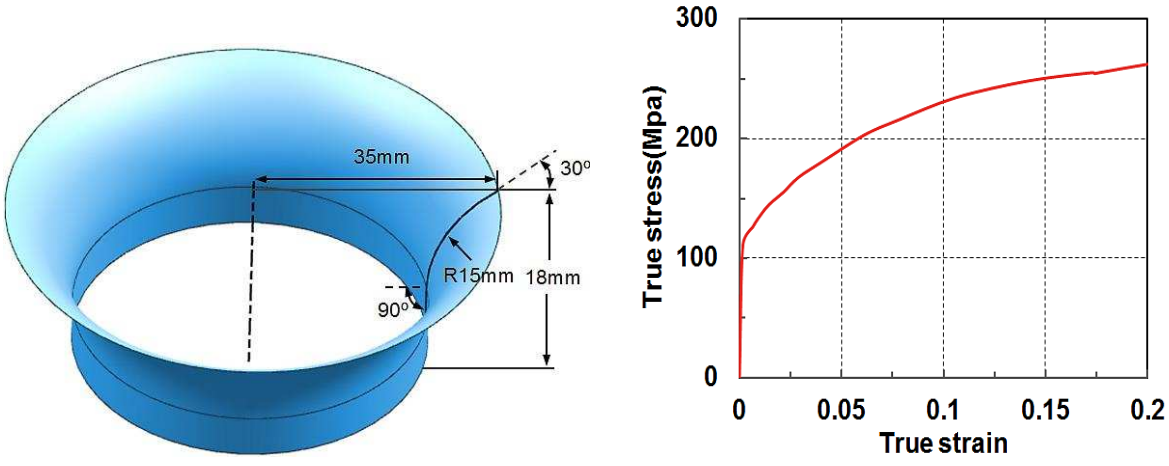

(a) designed shape (b) flow stress of AA5052 sheet metal

Fig. 7. Designed hole-flanging geometry and the material flow stress curve.

During numerical simulation, the commercial software LS-Dyna is used for the two ISF hole-flanging processes as shown in Fig. 8. To simplify the finite element simulation, the hole-cutting step is ignored and

a hole with initial diameter of 40 mm is defined in each finite element model. In addition, the geometry of T2 is simplified as shown in Fig. 8(b), in which only the geometric profile for flanging process is considered. Fully integrated 8-node S/R solid elements are utilized to discretize the blank, and 5 layers of solid elements are employed along the thickness direction of the sheet. Refine meshing strategy is used in the region to be formed to evaluate the simulation accuracy. Both the tool and the backing plate are regarded as rigid constraints. Coulomb's friction law is employed and the frictional coefficient between the forming tool and the sheet metal is assumed as 0.05 [27].

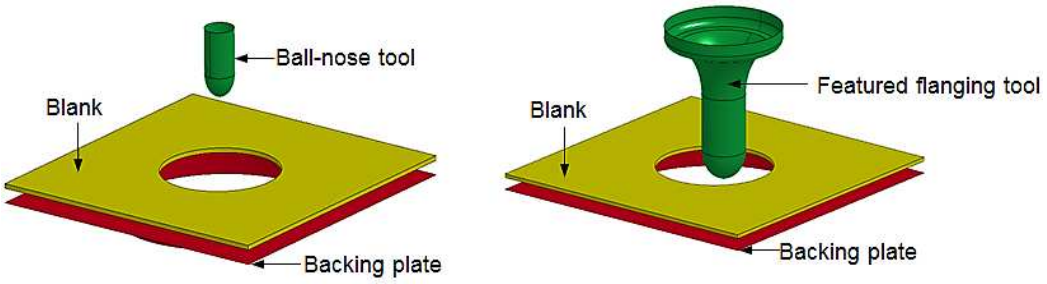

(a) T1 (b) T2

Fig. 8. Finite element models of two ISF flanging processes.

4.2 Analyses of simulation results

The effective strain distributions of the two hole-flanging processes are shown in Fig. 9(a) and (b), respectively. The maximum effective strain with T1 occurs at the 1/2 height of the flanged wall, which is obviously away from the hole edge. This is in consistent with the result obtained by Centeno et al. [18]. But for T2, the maximum value is at the hole edge. In addition, the maximum effective strain under T1 is higher, reaching a value of 0.6 compared with about 0.5 under T2. Fig. 9(c) and (d) give the final geometries of the two formed parts in the axial section after simulations. It can be seen that T1 could produce a taller flange than T2, but the thickness distribution under T2 is thicker and more uniform. To further explain the cause of such difference, Fig. 9(e) and (f) show the contact areas under two different tools. The tool-sheet contact area with T1 is quite small. According to the shape of deformed elements, it is found that stretching and bending deformations occur during the forming process. However, the contact area with T2 is much larger. As shown in Fig. 9(f), bending becomes a major deformation mode while the stretching is not obvious. Different modes of the contact and boundary conditions result in the varied sheet deformation modes and material flows around the tools.

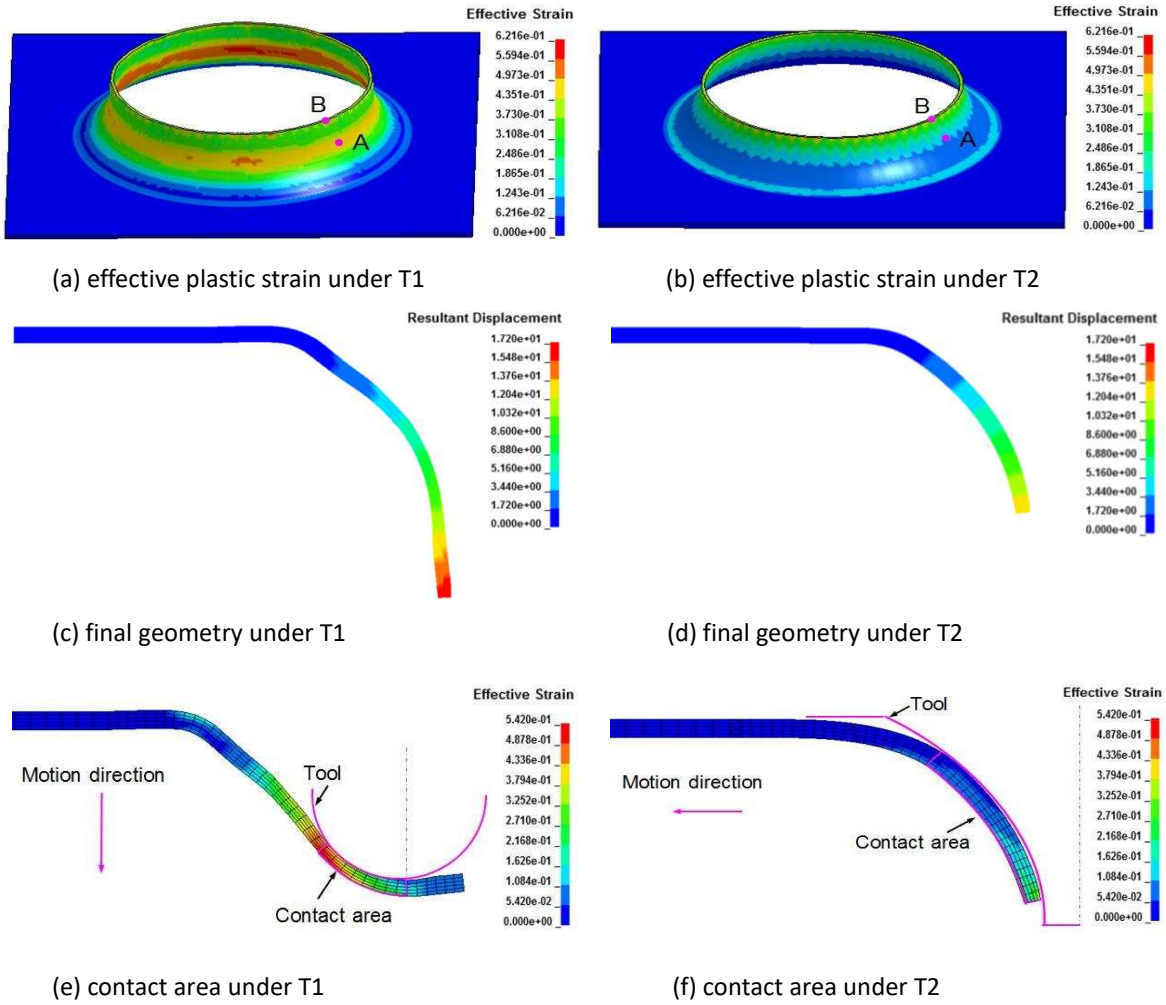

(a) effective plastic strain under T1

(b) effective plastic strain under T2

(c) final geometry under T1

(d) final geometry under T2

(e) contact area under T1

(f) contact area under T2

Fig. 9. Simulation results by using different forming tools.

To investigate the deformation mechanism of deforming sheet metal, the distributions of strain components along the meridional and circumferential directions are shown in Fig. 10. It is worth mentioning that the distance used in Fig. 10 is the initial distance before deforamtion. As shown in Fig. 10(a), the meridional strain under T1 increases from the top edge to a maximum value of 0.4 at the 1/2 height of the flanged wall while the circumferential strain starts to increase rapidly until reaching the hole edge. This indicates that the sheet metal has experienced uniaxial stretching deformation and approximately the plane-strain deformation mode before reaching the 1/2 height of the flanged wall. However, beyond the distance of 9 mm, the meridional strain starts to decrease. The deformation mode is changed from meridional stretching to circumferential stretching in this region. As shown in Fig. 10(b), the strain value in the meridional direction under T2 is relatively small with a negative value of around -0.1, which implies a compressive deformation state. This compressive deformation may be caused by tool squeezing the sheet metal during the forming process. Along the circumferential direction, the strain increases gradually to a value of about 0.33 at the hole edge. This result reveals a typical deformation state of hole-expansion. For both two hole-

flanging processes, the circumferential strains reach a similar value, while the meridional strain with T2 is much smaller.

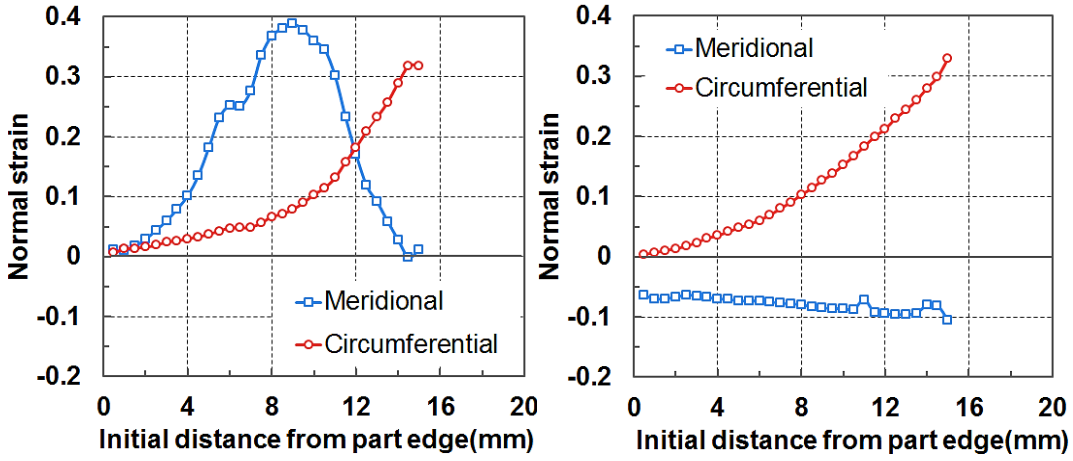

(a)T1 (b) T2

Fig. 10. Comparison of normal strain distributions.

To further reveal the difference of the two hole-flanging processes, the strain variations during each forming process are also investigated. Two points selected for tracing the variations are shown in Fig. 9: point A is located at the 1/2 height of flanged wall and point B is near the hole edge. As shown in Fig. 11(a) and (b), both the meridional strain and circumferential strain at point A under T1 increase first and keep almost unchanged due to the leaving of forming tool. However, the circumferential strain at point B increases gradually during the forming process, while the meridional strain decreases at first but then increases due to the continuous stretching in the circumferential direction and absence of any constraint at the hole edge. The absence of constraint and reduced meridional strain near the hole edge cause the occurrence of strain peak at the middle of the wall other than at the hole edge shown in Fig. 9(a). Concerning the strain variations in the hole-flanging process by T2 as shown in Fig. 11(c) and (d), both meridional strain and circumferential strain increase gradually at point *A* and point *B* during the forming process. This is because the tool is always keeping in contact with the forming area during the whole forming process, which causes the sheet metal to deform all the time. In addition, both meridional strain and circumferential strain at point *B* are greater than those at point *A*. This is because the tool moves from inward to outward during hole-flanging process using T2. Point *B* is at the first forming zone and the degree of deformation will accumulate until the forming process finishes.

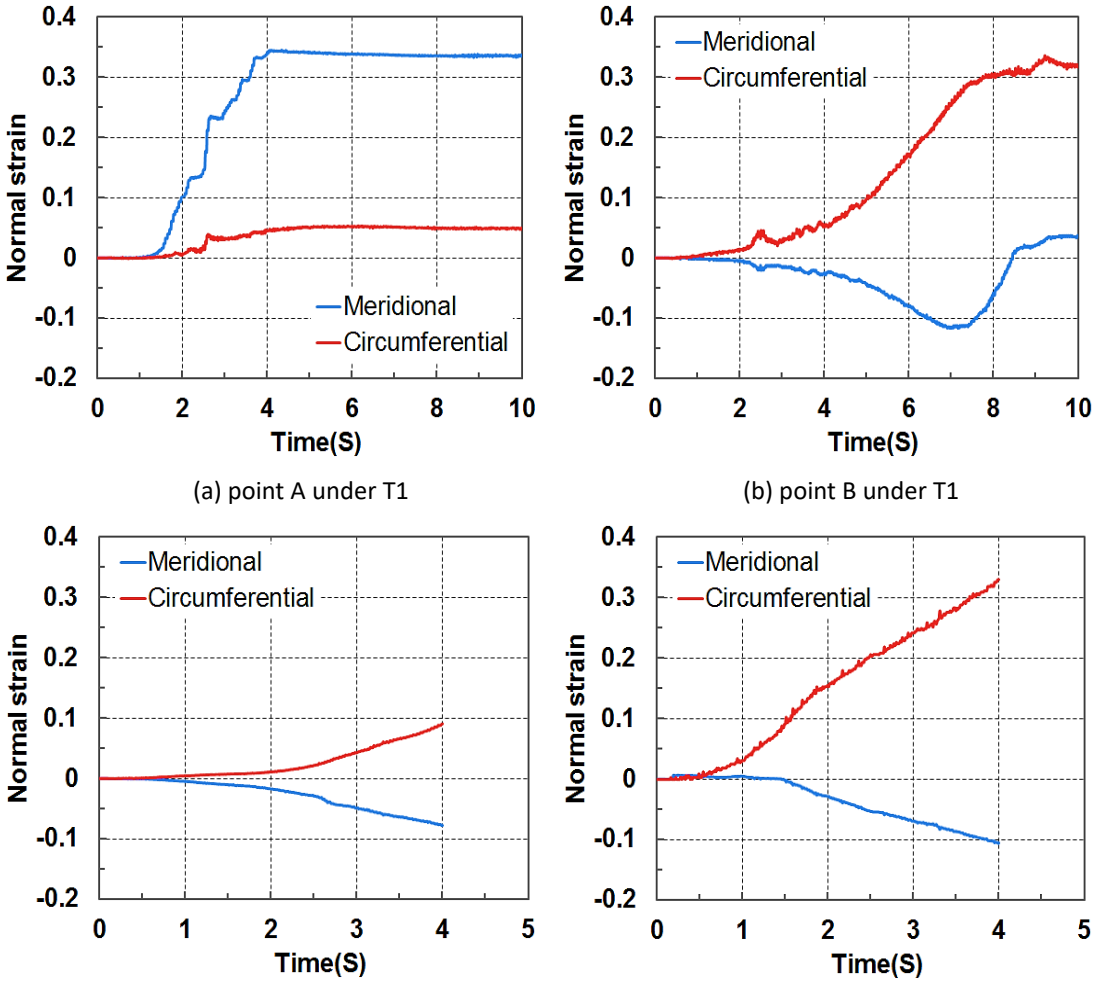

(a) point A under T1

(b) point B under T1

(c) point A under T2

(d) point B under T2

Fig. 11. Comparison of normal strain variations during hole-flanging.

Through-thickness shear is another unique deformation mode in ISF process. Shear strains in both meridional and circumferential directions are obtained as shown in Fig. 12. For the hole-flanging part made by T1, the maximum circumferential shear strain is observed at the middle position between the top edge and hole edge. However, the circumferential shear strain starts to decrease after this point, which may be due to the decreasing of contact stress and the corresponding frictional condition. Along the meridional direction, the magnitude of shear strain is relatively small during the whole process. However, the shear strain at the hole edge increases to a value of 0.1, which implies a considerable shearing deformation at the hole edge. This may be because that when the forming tool is approaching the hole edge, the absence of sheet material at the hole edge reduces the resistance of sheet metal deformation along the meridional direction. Meridional and circumferential shear strains under T2 are very small, which suggests limited shear deformation in the hole-flanging process.

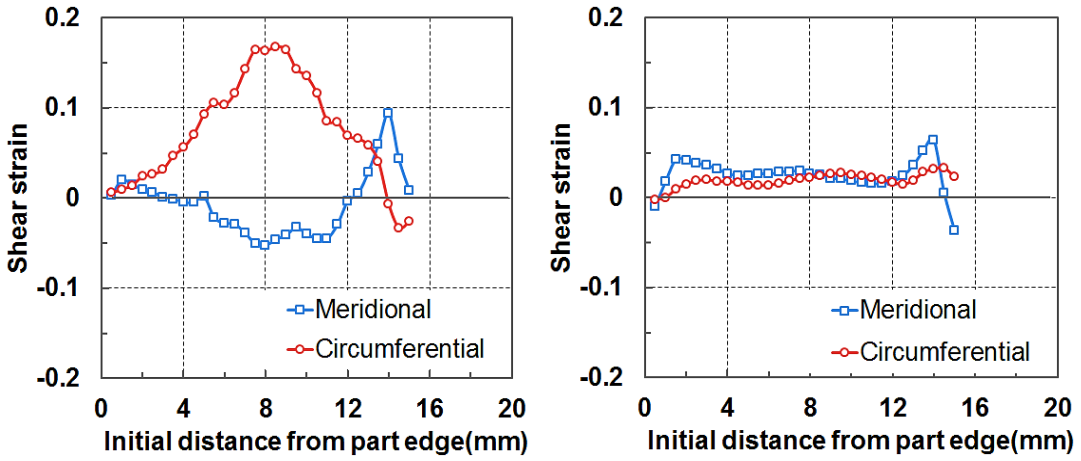

(a) T1 (b) T2

Fig. 12. Comparison of shear strain distributions.

Fig. 13(a) and (b) illustrate the variations of shear strains with time at the selected points under T1. Similar to the normal strains, the shear strains at point A increases to a certain value and keeps stable. While the meridional shear strain at point B decreases first and then increases. This may be due to the absence of constraint at hole edge and the bending & unbending of the sheet metal during the forming process. Fig. 13(c) and (d) show the variations of shear strain components under T2. It can be seen that the two shear strains at selected points A and B are much smaller than those under T1, which suggests that the point contact by T1 could generate larger shear strains than the “band” contact created by T2.

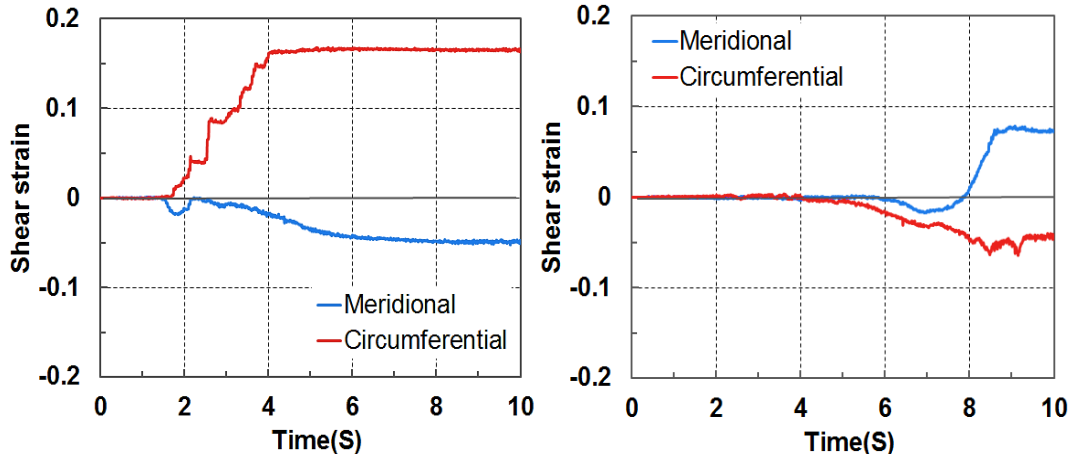

(a) point A under T1 (b) point B under T1

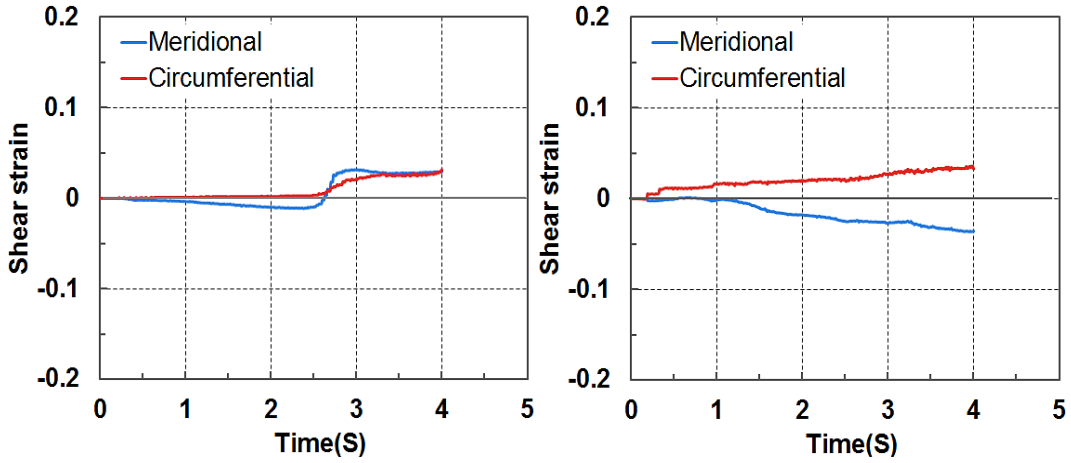

(c) point A under T2 (d) point B under T2

Fig. 13. Comparison of shear strain variations during hole-flanging.

5. Experimental investigations

5.1 Experimental test setup

Experimental tests are conducted to validate the geometric accuracy, thickness distribution, forming load, deformation mechanism and fracture behavior under each forming tool. In the experiments, a 3-axis CNC milling machine is employed to form the designed hole-flanging part. During each forming process, a back plate with a diameter of 70 mm is placed at the bottom of the sheet metal blank to avoid the bending of shoulder area as shown in Fig.14. The tool feed rate for each forming process is 2000 mm/min. During the forming process, grease is used as lubricant to reduce friction on the contact surface.

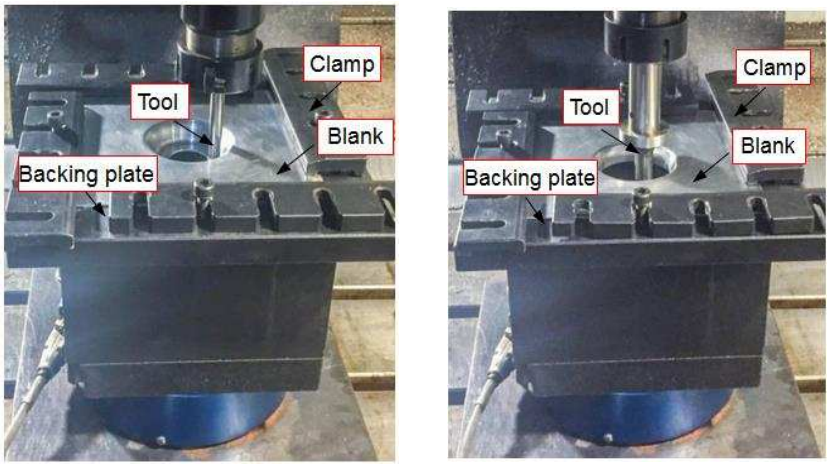

(a) T1 (b) T2

Fig. 14. Experimental setups.

5.2 Geometric accuracy and thickness distribution

The profiles of the final parts under two different tools are examined and shown in Fig. 15(a). It can be found that the produced flanges by both tools match well with the designed geometry, the maximum

deviation is less than 1 mm. The geometric deviation of the part formed by T2 is slightly larger than that by T1, it may be due to the larger bending deformation generated by T2. Bending may also result in larger springback. Furthermore, it is observed that there is obvious difference in forming depth of the two formed parts. The flanged part obtained by T1 can reach a depth of 16 mm whilst that under T2 is only about 12 mm.

Concerning the thickness distribution shown in Fig. 15(b), the minimum thickness of the hole-flanging part fabricated by T1 is about 0.58 mm while that obtained by T2 is 0.8 mm. In addition, T2 can achieve a more uniform sheet thickness distribution than that by T1. This result suggests that T2 could produce a shorter but thicker flange rim while that by T1 the flange is taller but thinner, confirming the results in Fig. 9.

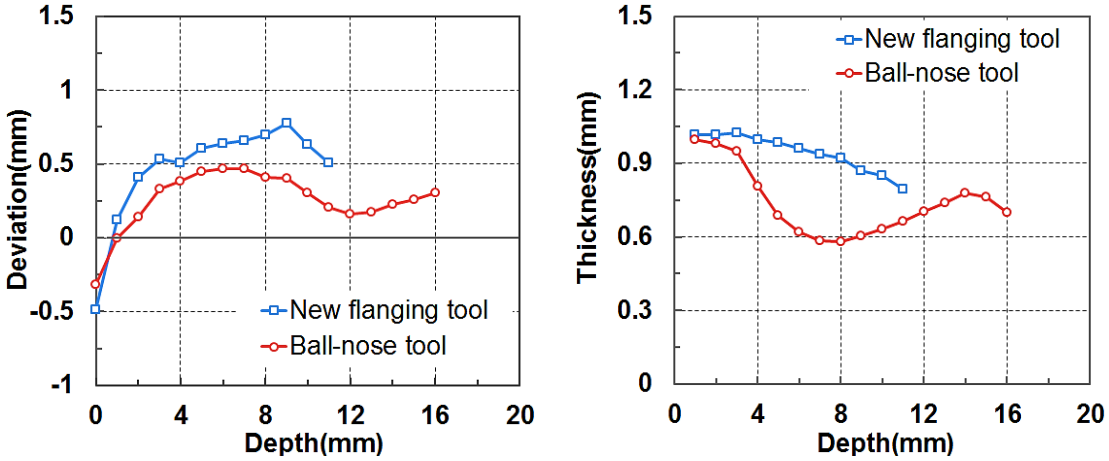

(a) shape deviation (b) thickness distribution

Fig. 15. Geometric deviation and thickness distribution.

5.3 Forming load

The forming load curves under T1 and T2 also show different patterns in variation as shown in Fig. 16. The horizontal load and vertical load under T1 increase at the initial stage and then reduce after a short period of constant stage. For T2 process the horizontal load and vertical load increase gradually during the whole forming process. Due to the “band” contact mode, the maximum forming load under T2 is about 30% higher than that of T1. Accordingly, higher forming load may result in an increased deflection and torque of the forming tool, which will affect the forming tool life and reduce the geometric accuracy of the part. To resolve this problem, the arm diameter of T2 that is independent with forming should be larger, e.g. twice as that of T1 in the present work. Therefore, the larger geometric deviation of the part formed by T2 in the previous section has less relationship with the deflection caused by the higher maximum forming load under T2. However, in both cases, the maximum forming load is less than 1000 N in each case, which is relatively small compared with the conventional hole-flanging process by punching.

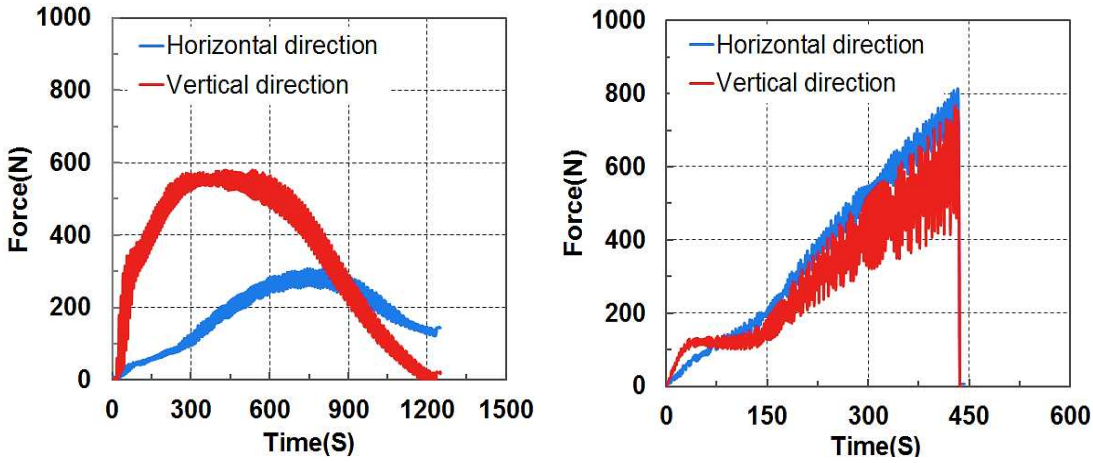

(a) T1 (b) T2

Fig. 16. Comparison of the forming load.

5.4 Sheet metal deformation behavior

In order to evaluate the sheet deformation mechanism, small circles with 1 mm diameter are prepared on the sheet surface by laser marker. After hole-flanging process, the initial circles are deformed into ellipses. Their lengths along major axis and minor axis are measured. By measuring the deformations of ellipses at point A and B, defined in the previous section, the meridional strain and circumferential strain in each process can be obtained as shown in Fig. 17. On the part made by T1 as shown in Fig. 17(a), the major deformation at point A is along the meridional direction, while that at point B is along the circumferential direction. The similar results were also observed by Centeno et al. [18] and Silva et al.[25]. In addition, the measured strains are very close to those obtained from finite element simulation as given in Fig. 10. On the part made by T2 shown in Fig. 17(b), negative meridional strains can be observed at both point A and B. The circumferential strain at point A is less than 0.1, while that for point B is about 0.3. These results are correlated well with the strain distributions obtained by numerical simulation.

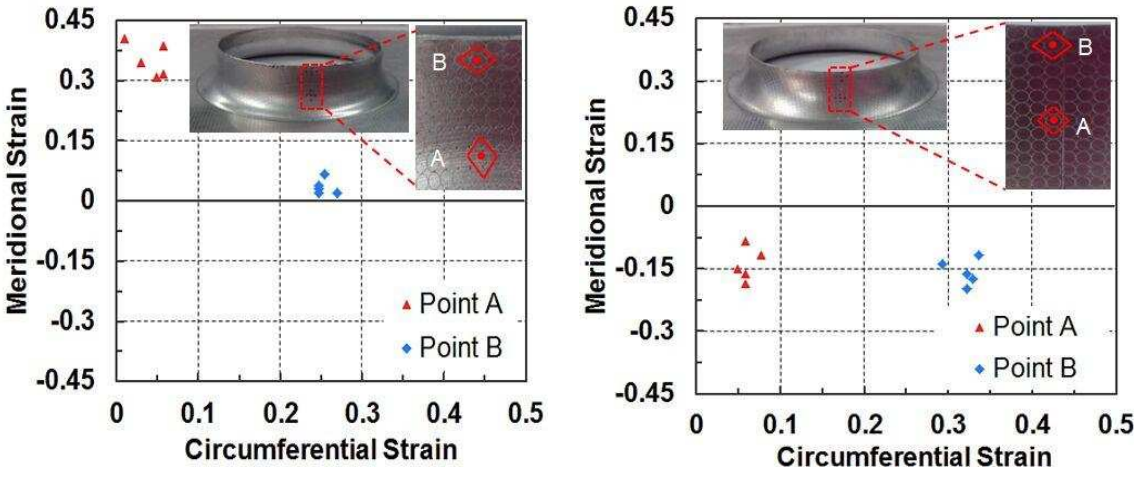

(a) T1 (b) T2

Fig. 17. The strain components at the selected positions.

The through-thickness shear deformation is also evaluated experimentally. Small holes with a diameter of 0.4 mm are drilled in the sheets by micro EDM before deformation as shown in Fig. 18(a). In this way, the deformation can be investigated by analyzing the deformed hole configuration. However, as the drilled hole at point B near the pre-cut hole will cause crack, only through-thickness shear at point A is investigated. On the part made by T1 as shown in Fig. 18(b) and (c), stretching can be observed in both meridional and circumferential directions, which are similar to the results in Fig. 10(a). In addition, bending can be observed along the meridional direction while shearing can be observed along the circumferential direction. This result is consistent with the observation in Fig. 12(a). For the part made by T2 given in Fig. 18(d) and (e), slight bending can be observed along the meridional direction. Along the circumferential direction, there is only limited stretching, which is consistent with the result in Fig. 10(b). However, no obvious shearing can be observed along the meridional direction and circumferential direction, which is also consistent with the observation in Fig. 12(b).

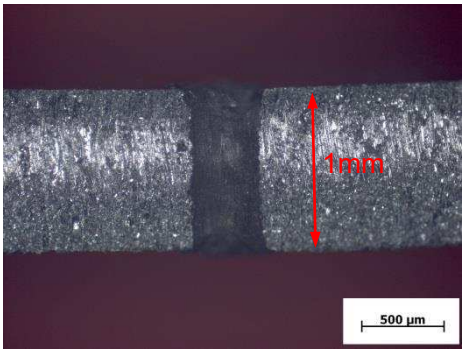

(a) initial hole

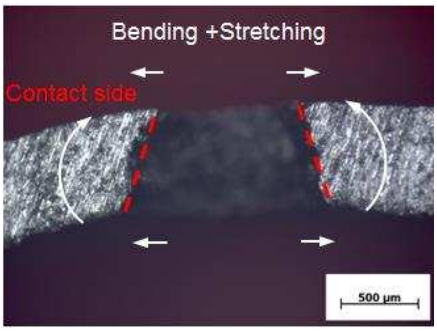

(b) meridional direction (T1)

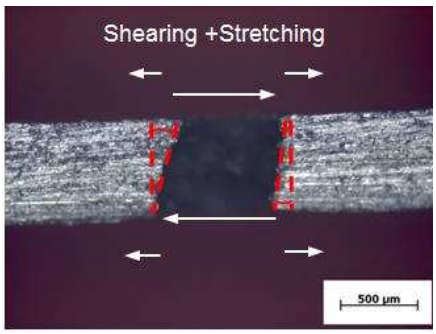

(c) circumferential direction (T1)

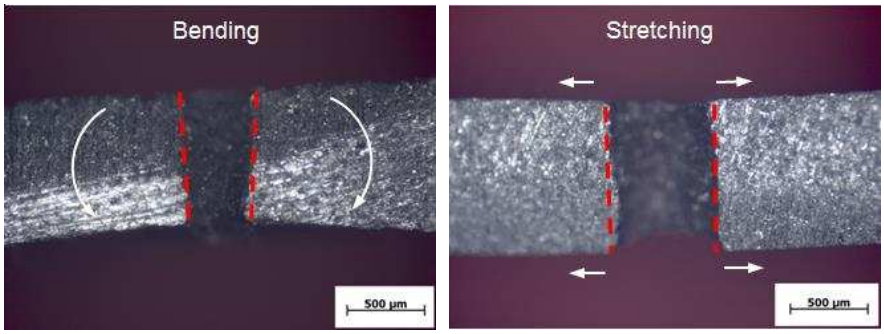

(d) meridional direction (T2) (e) circumferential direction (T2)

Fig. 18. The deformation of drilled holes before and after each forming process.

Fig. 19 shows the final formed parts by the two ISF hole-flanging processes, the forming depth of the part obtained by T1 is obviously higher than that obtained by T2. In addition, the shape of the hole edge is also quite different. Under T1, the inner surface of the flanged wall is much higher than the outer surface, which implies severe shear deformation along the meridional direction. However, under T2, no obvious shearing is observed at the hole edge.

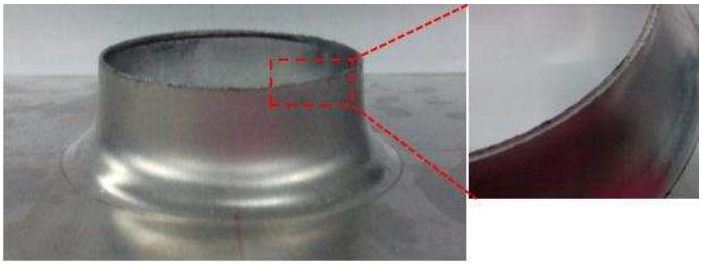

(a) T1

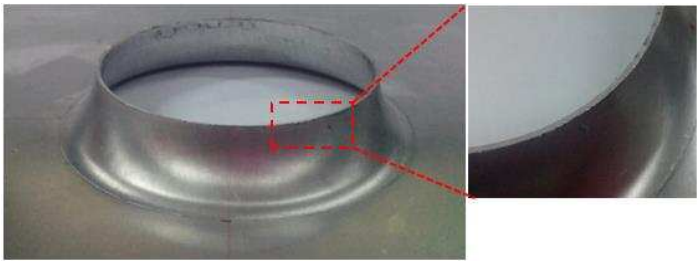

(b) T2

Fig. 19. Comparison of the final formed parts.

5.5 Fracture behavior

In order to obtain the fracture in the ISF hole-flanging process, a hole-flanging feature with larger expansion rate is specifically designed, as shown in Fig. 20. This feature cannot be directly achieved by using either T1 or T2 due to deeper vertical wall compared with that shown in Fig. 7(a). In this way, the fracture

behavior in each process can be investigated.

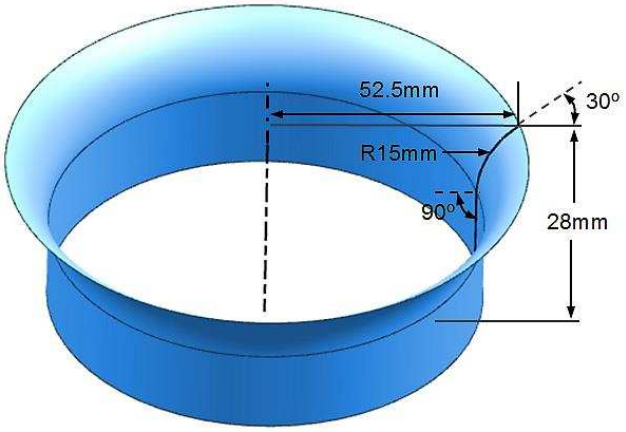

Fig. 20. The designed geometric profile for fracture analysis.

By adopting one single pass ISF strategy described in Fig. 2, the fractured parts are obtained shown in Fig. 21. Fig. 21(a) shows the fractured part under T1 with the forming angle reaching about 82º and the forming depth of 11 mm. The fracture under T1 occurs horizontally on the inclined wall and away from the hole edge, which is similar to conventional ISF process due to the maximum principal stress along the meridional direction. The cross-section of the fracture area shows that the fractured thickness is reduced from 1.0 mm to 0.21 mm with slight necking. While under T2, the fracture occurs at the hole edge vertically due to the maximum principal stress in the circumferential direction. The forming angle reaches 90º and the forming depth is 21 mm, as shown in Fig. 21(b). The cross-sectional shape of the fracture area shows the fracture thickness is reduced from 1.0 mm to 0.25 mm with greater necking, which is slightly higher than that of T1. The fracture location on each part confirms to the distribution of stress triaxiality by the analytical model under T1 and T2 in Fig.6.

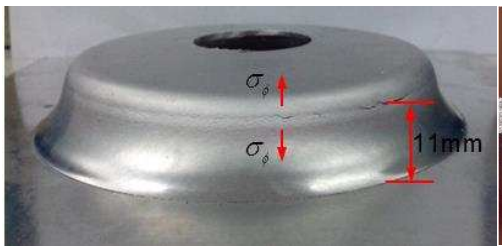

(a) fracture part under T1

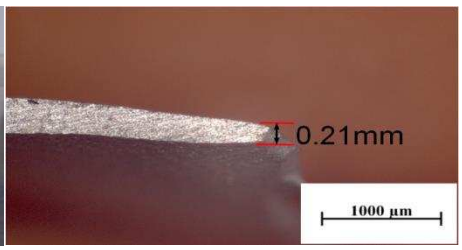

(b) cross-section of fracture area under T1

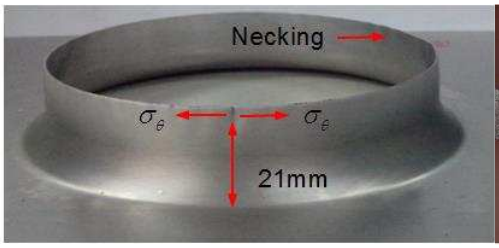

(c) fracture part under T2

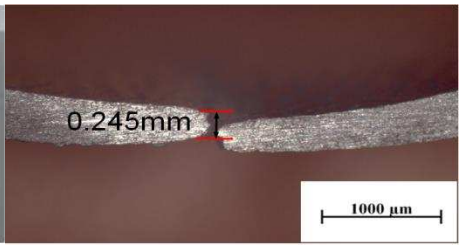

(d) cross-section of fracture area under T2

Fig. 21. Comparison of fractures and necking behaviors.

To further investigate the fracture mechanism, multi-pass hole-flanging strategy is implemented using T1 until fracture occurs. During the process as shown in Fig. 22 (a), the vertical step value of 0.1 mm and the gap value of 0.5 mm between two passes are used. For T2 as shown in Fig. 22(b), only one pass with the same step value is employed. The hole-expansion ratio *R*, as an indicator of the forming limit, is calculated and compared for these two processes by using Eq. (25):

$$R = (D - D_0)/D_0 \tag{25}$$

where the diameter of the pre-cut hole (D_0) is 40 mm, and D is the final achieved diameter.

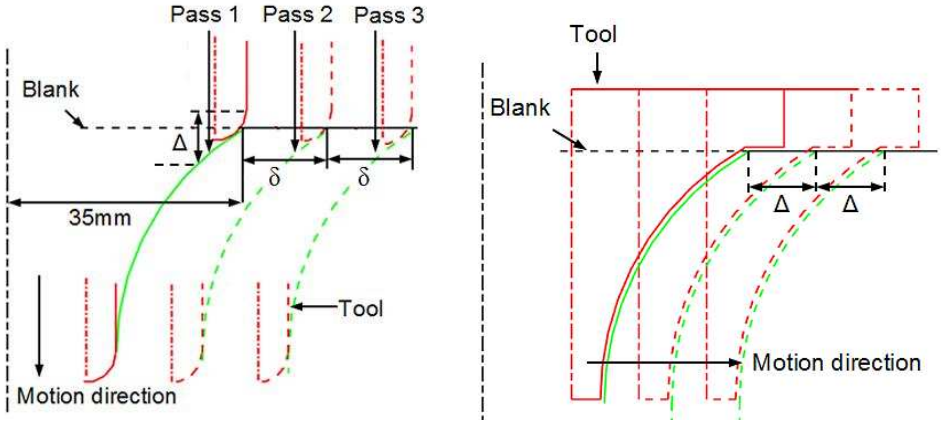

(a) T1 (b) T2

Fig. 22. Hole-expansion illustration by two different hole-flanging tools.

The fracture occurs vertically during multi-pass ISF under T1, and the forming depth is obviously higher as shown in Fig. 23. The final diameter is 60 mm, i.e. the hole-expansion ratio is 50%. However, the final diameter is 86 mm under T2 with a higher hole-expansion ratio of 115%. This result suggests that even using T1 with the multi-pass strategy, the forming limit is still much lower when compared with T2 using only one forming pass.

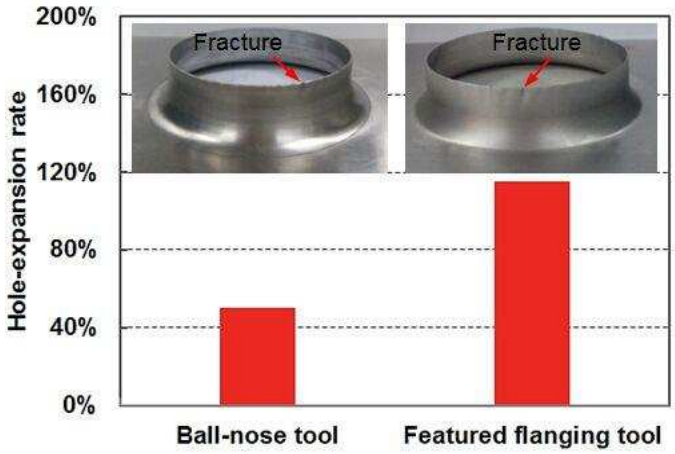

Fig. 23. Hole-expansion comparison between the two hole-flanging processes.

The difference of hole-flanging fracture behaviors under T1 and T2 can be explained by the varied deformation mechanisms. Under T1, the contact between the tool and the sheet metal is local, causing stress concentration. Although the tool with small radius could increase the deformation stability, while with the spiral tool path going downwards, the sheet is unavoidably stretched along the meridional direction and becomes thinner. Under T2 the contact between the tool and the sheet metal is in a narrow “band”. Although the radius of T2 is larger and deformation is less stable than T1, the meridional stretching can be avoided and the major deformation is along the circumferential direction. This deformation mode is similar to the conventional hole-flanging process by hole punching, but advantageous for ISF flanging is the enhanced flexibility due to localized deformation.

5.6 Discussions

By changing the key geometry of the ISF flanging tool with a concave arc section, a different contact and boundary conditions can be obtained under T2 in ISF based hole-flanging process. The “band” contact replaces the point contact using the conventional ISF tool. Benefited from this new type of contact condition, the sheet metal can be bent and expanded other than extremely stretched. The new deformation mode may result in different forming shape, thickness distribution and forming load in the ISF flanging process. Specifically, extreme thinning can be avoided under T2. However, due to the volume conservation principle, the thicker walled flange means a reduced height of the flange.

Different from T1, T2 could generate a different sheet deformation mode. In the area far away from the pre-cut hole, bending along the meridional direction is the dominant deformation mode. However in the area near the hole, the major deformation mode is shifted to circumferential stretching. Under T1, for the region

far away from the pre-cut hole, the meridional stretching and the circumferential through-thickness shear are the main deformation mode, which is the same as conventional ISF deformation observed by Lu et al [26]. However, when the tool approaches the hole edge, the dominant deformation becomes circumferential stretching and meridional shearing, which is different from the conventional ISF process. The varied deformation model accounts for the difference of the parts obtained by T1 and T2 in the aspects of geometry, thickness distribution and forming load.

The improved formability under T2 results in a greater hole-expansion ratio indicating an improved formability. With bending at initial forming stage, the over-stretching can be avoided, and the final hole-expansion ratio is much higher than that by T1 even when using multi-pass tool path strategy. The investigation in this work suggests that T2 has obvious advantages compared with T1. Less forming steps are required with improved forming efficiency under T2. In addition, a milling cutter can be designed at the tool head to prepare the pre-cut hole without the need of changing the tool, and the forming load is still within the acceptable range of machining center. This means that conventional ISF forming equipment such as NC milling machine or robot can also be used for the new hole-flanging process by using T2.

Concerning the disadvantages of T2, the tool radius needs to match the designed geometry of the flange, and this will reduce the process flexibility. Another potential problem is forming the flange feature with a small radius, in which the sheet metal may not be directly bent under the small concave radius. In order to solve this problem, multi-pass hole-flanging strategy may be used as a potential solution, to generate a preform hole flange feature with a larger radius first and then to gradually reduce this radius by repeating the same process but using another tool with smaller radius.

6. Conclusions

In the present work, a new ISF flanging tool has been developed and validated. Based on the comparative studies by analytical modeling, numerical simulation and experiment, the unique deformation mode under the new flanging tool has been characterized. The conclusions are summarized as follows.

Compared with the traditional tool, the new tool results in more varied stress state which is sensitive to the process parameters.

Circumferential stretching and meridional bending deformation occur during the hole-flanging process, and the tool-sheet contact area under the new tool is much larger.

Less obvious through-thickness shearing deformation can be observed under the new tool.

The new tool can form part with more uniform thickness distribution, and avoid extreme thinning

caused by the traditional tool.

The new flanging tool increases the hole-expansion ratio by 130%.

Acknowledgement

The authors acknowledge the support provided by the EU FP7 Marie Curie International Incoming Fellowship FLEXFORM project (628055 & 913055) and International Research Staff Exchange Scheme MatProFuture project (318968).

References

[1] Y.I. Baldin, Y.I. Shein, Y.I. Berliner, V.M. Brif, Y.I. Rubenchik, Flanging of holes in bodies of cylindrical apparatus, Chem Petrol Eng 5 (1969) 302-304.

[2] W. Johnson, N.R. Chitkara, A.H. Ibrahim, A.K. Dasgupta, Hole-flanging and punching of circular plates with conically headed cylindrical punches, The Journal of Strain Analysis for Engineering Design 8 (1973) 228-241.

[3] T. Kumagai, H. Saiki, Deformation analysis of hole-flanging with ironing of thick sheet metals, Metals and Materials 4 (1998) 711-714.

[4] T. Kumagai, H. Saiki, Y. Meng, Hole-flanging with ironing of two-ply thick sheet metals, Journal of Materials Processing Technology 89–90 (1999) 51-57.

[5] M.J. Worswick, M.J. Finn, The numerical simulation of stretch flange forming, International Journal of Plasticity 16 (2000) 701-720.

[6] P. Groche, R. Erhardt, Lasererwärmung zur Verbesserung des Umformergebnisses beim Kragenziehen von Aluminium- und Magnesiumknetlegierungen, Materialwissenschaft und Werkstofftechnik 35 (2004) 467-472.

[7] G.D. Head, W.C.L. Master, L.P. Bredesky, D.C. Winter, For forming a hole and a brushing in a metal workpiece, Google Patents (1984).

[8] S. Miller, A. Shih, Friction Drilling: A Chipless Hole-Making Process, ASME 2006 International Manufacturing Science and Engineering Conference (2006) 911–918.

[9] J.M. Allwood, D.R. Shouler, Paddle Forming: A Novel Class of Sheet Metal Forming Processes, CIRP Annals - Manufacturing Technology 56 (2007) 257-260.

[10] J.M. Allwood, D.R. Shouler, Generalised forming limit diagrams showing increased forming limits with non-planar stress states, International Journal of Plasticity 25 (2009) 1207-1230.

[11] R. Malhotra, L. Xue, T. Belytschko , J. Cao, Mechanics of fracture in single point incremental forming, Journal of Materials Processing Technology 212 (2012) 1573-1590.

[12] T. Teramae, K. Manabe, K. Ueno, H. Takeda, Effect of material properties on deformation behavior in incremental tube-burring process using a bar tool, Journal of Materials Processing Technology 191 (2007) 24-29.

[13] Z. Cui, L. Gao, Studies on hole-flanging process using multistage incremental forming, CIRP Annals-Manufacturing Technology 2 (2010) 124-128.

[14] A. Petek, K. Kuzman, Backward hole-flanging technology using an incremental Approach, Journal of Mechanical Engineering 58 (2012) 73-80.

[15] C. Yang, T. Wen, L.T. Liu, H. Wang, Dieless incremental hole-flanging of thin-walled tube for producing branched tubing, Journal of Materials Processing Technology 214 (2014) 2461-2467.

[16] M. Bambach, H. Voswinckel, G.Hirt, A new process design for performing hole-flanging operations by incremental sheet forming, Procedia Engineering 81 (2014) 2305-2310

[17] G. Centeno, B. Silva, C. Vallellano, P. Martins, Manufacturing of Sheet Metal Flanged Parts using Multi-stage SPIF, Metal Forming 2012 - The 14th International Conference on Metal Forming (2012) 271-274.

[18] G. Centeno, M.B. Silva, V.A.M. Cristino, C. Vallellano, P.A.F. Martins, Hole-flanging by incremental sheet forming, International Journal of Machine Tools and Manufacture 59 (2012) 46-54.

[19] L. Montanari, V.A. Cristino, M.B. Silva, P.A.F. Martins, A new approach for deformation history of material elements in hole-flanging produced by single point incremental forming, The International Journal of Advanced Manufacturing Technology 69 (2013) 1175-1183.

[20] V.A. Cristino, L. Montanari, M.B. Silva, A.G. Atkins, P.A.F. Martins, Fracture in hole-flanging produced by single point incremental forming, International Journal of Mechanical Sciences 83 (2014) 146-154.

[21] V.A.M. Cristino, L. Montanari, M.B. Silva , P.A.F Martins, Towards square hole-flanging produced by single point incremental forming, Proceedings of the Institution of Mechanical Engineers, Part L: Journal of Materials Design and Applications (2014) 1-9.

[22] M.B. Silva, T.M. Martinho, P.A.F. Martins, Incremental forming of hole-flanges in polymer sheets, Materials and Manufacturing Processes 28 (2013) 330-335.

[23] S.A. Yonan, M.B. Silva, P.A. Martins, A. Tekkaya, Plastic flow and failure in single point incremental forming of PVC sheets, Express Polymer Letters 8 (2014) 301-311.[24] V. Cristino, M.B. Silva, P. Wong, L. Tam, P.A. Martins, Hole-flanging of metals and polymers produced by single point incremental forming, Int. J. Materials and Product Technology 50 (2015) 37-48.

[25] M.B Silva, P. Teixeira, A. Reis, P.A Martins, On the formability of hole-flanging by incremental sheet forming,

Proceedings of the Institution of Mechanical Engineers, Part L: Journal of Materials: Design and Applications 227 (2013) 91-99.

[26] B. Lu, Y. Fang , D.K. Xu , J. Chen , H. Ou, N. H. Moser, J. Cao , Mechanism investigation of friction-related effects in single point incremental forming using a developed oblique roller-ball tool, International Journal of Machine Tools and Manufacture 85 (2014) 14-29

[27] P. Eyckens, B. Belkassem, C. Henrard, J. Gu, H. Sol, A.M. Habraken, J.R. Duflou, A.V. Bael, P.V. Houtte, Strain evolution in the single point incremental forming process: digital image correlation measurement and finite element prediction, International Journal of Material forming 4 (2011) 41-75.